Atmospheric Research 302 (2024) 107308

Contents lists available at ScienceDirect

Atmospheric Research

journal homepage: www.elsevier.com/locate/atmosres

Detection and characterization of hailstorms over France using DPR data onboard the GPM Core Observatory

Laura Rivero-Ordaz [a,*], Andrés Merino [a], Andrés Navarro [b], Francisco J. Tapiador [b], José L. Sánchez [a], Eduardo García-Ortega [a]

[a] Atmospheric Physics Group (GFA), Environmental Institute, Universidad de León, 24071 León, Spain
[b] University of Castilla-La Mancha (UCLM), Institute of Environmental Sciences (ICAM), Faculty of Environmental Sciences and Biochemistry, Earth and Space Sciences (ESS) Group, Avda. Carlos III s/n, Toledo 45071, Spain

ARTICLE INFO

Keywords:
Detection of hailstorms
Hailpad network
DPR
GPM

ABSTRACT

Hailstorms cause heavy losses, especially when their hailstones reach a large size. One of the European regions most affected by these severe atmospheric events is southern France, where a valuable and extensive hailpad network has been operational for more than three decades. These direct observations are extremely useful because they allow for the definitive verification of hailfall at the ground. Space-based sensors have seen increasing importance in hail monitoring. Global Precipitation Measurement (GPM) is an international mission designed to advance precipitation measurements from multispectral sensors. The GPM core satellite carries a powerful and unprecedented Dual-Frequency Precipitation Radar (DPR) for studying 3D precipitation characteristics. The objective of the present study is to evaluate the DPR sensor ability to identify hailstorms. We identified eight hailstorms over France where DPR data were coincident with ground-based observations from a hailpad network during 2014–2021. In addition, variables provided by the DPR sensor indicative of hail presence were studied and five detection algorithms were tested. This research serves as background for future work and the development of prediction algorithms based on empirical relationships with GPM data.

1. Introduction

Severe weather events, particularly hailstorms with large hydrometeors, cause heavy losses worldwide. In much of Europe, hailstorms have a marked socioeconomic impact because they cause economic losses of billions of euros and can put human lives at risk (Punge and Kunz, 2016; Ni et al., 2017; Bang and Cecil, 2019). The Mediterranean area generally has a high frequency of hail (Marra et al., 2017). The south of France is one of the European regions most affected by these hydrometeors and is also one of the most studied because an extensive network of detection devices that has been in operation there for more than three decades (Hermida et al., 2013; Sánchez et al., 2017).

The local nature and short duration of hailstorms mean that both their prediction and detection remain problems (Smith and Waldvogel, 1989; Kunz, 2007). Hail develops in convective cells that have a limited spatiotemporal extent. Therefore, they are not generally detected by synoptic stations (López and Sánchez, 2009). To forecast this phenomenon it is necessary to consider the physical mechanisms involved in convection and concurrent meteorological conditions (Doswell III, 1987; Johns and Doswell III, 1992).

Hail detection has been a major limitation to advances in prediction (Toker et al., 2021). For a long time, databases on hailfalls and hail characteristics were from networks of volunteer observers (Sánchez et al., 2009) that, despite their subjectivity and lack of spatial homogeneity, have been used to validate various studies (López and Sánchez, 2009). In addition, newspaper archives and records of insured damages have made it possible to carry out climatological studies or investigate unique cases of powerful impacts. Another direct observation tool is the use of hailpad networks such as the one in France belonging to the Association Nationale d'Etude et de Lutte contre les Fléaux Atmosphériques (ANELFA). These networks have been very useful in research owing to the information they provide, although their lack of standardization is a drawback (Punge and Kunz, 2016; Sánchez et al., 2017).

Undoubtedly, a significant advance in detection was the incorporation of terrestrial radars (Mroz et al., 2017). Various radar parameters have been used to identify hailstorms (López and Sánchez, 2009).

* Corresponding author.
E-mail addresses: lrivo@unileon.es (L. Rivero-Ordaz), andres.merino@unileon.es (A. Merino), andres.navarro@unileon.es (A. Navarro), francisco.tapiador@uclm.es (F.J. Tapiador), jl.sanchez@unileon.es (J.L. Sánchez), eduardo.garcia@unileon.es (E. García-Ortega).

https://doi.org/10.1016/j.atmosres.2024.107308
Received 12 July 2023; Received in revised form 16 February 2024; Accepted 24 February 2024
Available online 27 February 2024

Motivated by the advantages of these sensors, the scientific community has worked on more precise detection algorithms (Mroz et al., 2017). Examples of these are Donaldson Jr. (1959), Waldvogel et al. (1979), Auer Jr. (1994), Kitzmiller et al. (1995), and Witt et al. (1998). More recent works, including Heinselman and Ryzhkov (2006), Depue et al. (2007) and Ortega et al. (2016), took advantage of the polarimetric capabilities of new sensors. However, the main disadvantage of these systems is their limited spatial coverage for monitoring hailstorms (Marra et al., 2017).

In general, surface observations have limited spatial coverage plus data biases and inconsistencies from a lack of standardization. It is necessary to have large databases both temporally and spatially to study the climatological behavior of hailstorms. With such information, patterns of occurrence and changes in frequency and intensity of these events can be more accurately defined. Attempting to overcome these limitations, a recent focus has been on the use of satellite data (Ni et al., 2017; Bang & Cecil, 2019 and 2021).

Currently, observations made using satellite sensors have the fundamental objective of studying more effectively the heterogeneity of the spatiotemporal patterns of precipitation (Kidd and Levizzani, 2011; Kidd et al., 2017; Marra et al., 2017; Michaelides, 2019). The Global Precipitation Measurement (GPM) mission is a benchmark and was considered by Laviola et al. (2020) as a powerful and unprecedented tool to monitor hailstorms. This mission is considered the successor to the successful Tropical Rainfall Measuring Mission (TRMM), allowing spatial expansion of observations to a range of ±65° latitude (Ni et al., 2017).

The GPM has a central observatory, the GPM Core Observatory

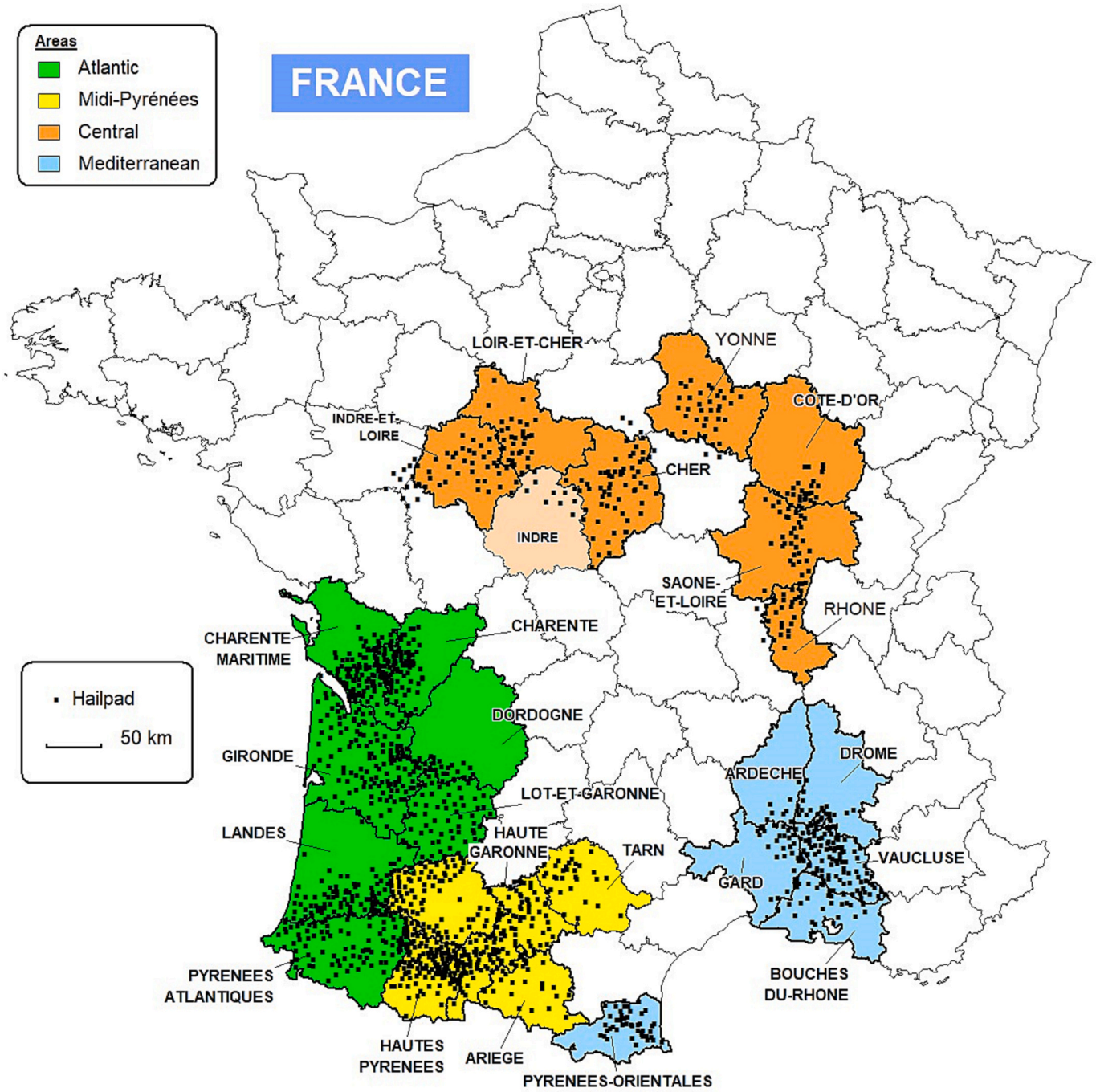

Fig. 1. Network of hail gauges across four regions of France (ANELFA).

(GPM-CO), which was launched on February 27, 2014 (Hou et al., 2014). The GPM-CO is equipped with two sensors. The first is the GPM Microwave Imager (GMI), a conical-scanning passive microwave radiometer, which enables the Core spacecraft to serve as both precipitation and radiometric standards for the other satellites. The other sensor is the first Dual-Frequency Precipitation Radar (DPR) in space. This advanced onboard system improves the accuracy of precipitation estimation and facilitates the analysis of cloud microphysical structure (Panegrossi et al., 2016; Le and Chandrasekar, 2021a).

Several studies have used GPM sensors to analyze hailstorm occurrence and improve their prediction, including Mroz et al. (2017 and 2018), Marra et al. (2017), Seiki (2021) and Le & Chandrasekar (2021a and 2021b). In these articles, most of the selected case studies were validated by terrestrial radar networks. However, hailpad networks provide a very complete and reliable "ground truth" (Sánchez et al., 2017). In the present work, a hailpad network was used for hailfall identification, using data from $>$ 1000 sensors during eight field campaigns in the south of France. Given this, the objective of the present work was to evaluate the DPR sensor capability in identifying hailstorms.

2. Study area and database

To conduct our research, the region covered by the ANELFA hailpad network in France was chosen as the study area. The detection network has been in operation since 1988 (Berthet et al., 2013; Melcón et al., 2017) and is expanded annually by the installation of new measurement stations. There are currently ~1500 hailpads. During campaigns, network technicians oversee the provision of information on the location, date, start time, and duration of hailfalls. The hailpads are delivered to ANELFA for image software analysis of hail characteristics such as diameter and number of impacts. The hailpad network extends across four regions (Fig. 1): the Atlantic zone, Pyrenees, central zone and Burgundy, and the southeast Mediterranean (Façade Atlantique, Midi-Pyrénées, Centre & Bourgogne, and Sud-Est Méditerranée).

Reports from annual ANELFA campaigns were used to obtain hailfall data over the study area. Direct observation data from the network were used to verify hailfall and identify storms over the region of France using the DPR sensor. Therefore, the study period began in 2014, when GPM-CO data became available operationally (provided by the National Aeronautics and Space Administration, NASA, and Japan Aerospace Exploration Agency, JAXA), through 2021, given the availability and processing of data from the hailpad network. In general, the GPM provides various products that are processed by the Precipitation Processing System and are available to the scientific community from the Goddard Earth Sciences Data and Information Services Center (GES DISC). Thus, various products were extracted from version 07 to characterize the identified storms.

We used data from the level-2A DPR product, suitable for investigating DPR detection capacity. This sensor furnishes profiles of 3D atmospheric structure and consists of two precipitation radars: Ku band (13.6 GHz) to detect intense and moderate rain and Ka band (35.6 GHz) to sense light rain and snow. The footprint diameter gives a 5-km horizontal resolution for both radars. The Ku band swath widths extend 245 km and that of the Ka band between 120 and 125 km of the interior region. Both radars have a nominal vertical range resolution of 250 m, sampled every 125 m. In the inner overlapping swath, measurements were made synchronously with dual frequency, whereas in the outer swath region, there were only Ku band observations. This scan pattern was modified on May 21, 2018, so that the dual-frequency algorithm was applied to the entire observation swath (Hou et al., 2014; Mroz et al., 2017 and 2018). Variables from the 2ADPR product are distributed in two file structures, Full Scans (FS) and High-Sensitivity Scans (HS). The FS structure contains data for both frequencies, whereas the HS structure provides the high-sensitivity data recorded by the Ka band. In our study, variables extracted from the FS structure were used.

2.1. Methodology

The hailfall database was extracted from ANELFA campaign reports. This included 2387 records across the eight years (2014–2021; Table 1). The JAXA GPM Quick Look system was also used, which provides and archives the GPM-CO observations. This system made it possible to identify annual DPR scans coinciding with the hail days in the initial direct observation database. A total of 187 DPR scans over France were found for recorded hailstorm days. Using these days and the coordinates of hailpad impacts, the DPR observation files were searched in GES DISC (Iguchi and Meneghini, 2021). We thereby identified eight hailstorms matched by DPR scans that covered the locations of one or more hailpads (totaling 26). The storm analysis was of the main convective cell observed by the DPR, confirming hail at the surface via hailpads. The study area analyzed for each storm had a different extent and is shown in Table 3. In the selected cases, a maximum time lag between estimated surface hailfall and the DPR measurements over the study area was ±50 min (Supplementary Tables 1–8), yielding a total of 26 hailpads for the eight identified storms. This time lag was considered acceptable because of the following: owing to small temporal uncertainties in the ANELFA reports, the lag between hail formation in the convective cell and its surface fall, and the time over which the storm could move outside the DPR swath.

Subsequently, we extracted different variables of the 2ADPR product. The variables were chosen based on the published background of the subject because previous works have demonstrated the utility of certain parameters for hailstorm forecasting. Finally, from the FS structure, maximum values of the following variables were extracted from the study area of each storm: Precipitation Rate Near Surface (PRNS, mm/h), Corrected Reflectivity Factor Near Surface (zFFNS, dBZ), and the Vertical Profile of the Corrected Reflectivity Factor (zFF, dBZ). Additionally, other variables were calculated from DPR data such as the Height of Maximum Reflectivity (HMR, m) and Maximum Heights of Reference Reflectivities (MHRR, m). The reference reflectivities were 40, 45, and 50 dBZ (MHR40, MHR45 and MHR50, m). Moreover, we determined the distance between the maximum heights of reference reflectivities and heights of the 0° and − 10 °C isotherms (DMH40, DMH45 and DMH50, m). The surface hail characteristics from ANELFA were also analyzed. For each storm, we ascertained the maximum value of each direct observation variable corresponding to one of the impacted plates coinciding with the DPR swath. These were the maximum diameter (mm), maximum total number (m^{-2}), maximum mass (kg/m^2), and maximum kinetic energy of fall (J/m^2). The kinetic energy E (J/m^2) measured by a hailpad is determined from the number of hailstones n_i (m^{-2}) in the diameter intervals ΔD_i with mean diameter D_i (mm), according to

$$E = 4,58x10^{-6}\sum_{i=1}^{p} n_i D_{i,}^4$$

where index p denotes the number of diameter intervals used. The global kinetic energy of a hailfall is defined as the sum of all the kinetic energies

Table 1
Hailstorms matched by DPR scans and registered by ANELFA.

Study years	*Records (hailpads impacted)*	*DPR scans over France on days with records*	*Records matched by DPR scans*	*Hailstorms matched by DPR scans*
2014	337	23	9	1
2015	160	10	5	1
2016	239	14	2	2
2017	313	27	3	2
2018	513	44	7	2
2019	313	13	0	0
2020	231	9	0	0
2021	281	47	0	0
Total	2387	187	26	8

measured by hailpads impacted by one hailfall. More detailed procedures on how to obtain the kinetic energy from hailpad measurements are described by Waldvogel et al. (1978).

Thereafter, we evaluated five hail detection algorithms that included variables from the DPR sensor (Table 2), as determined by Mroz et al. (2017). Radiosonde data were used to determine isotherm heights. The 12 UTC radiosonde nearest the location of the impacted hailpads was selected because it is representative of the pre-convective environment (López et al., 2007). Measured reflectivity was used in the algorithm calculations, as suggested by Mroz et al. (2017). This variable was used to avoid errors that may arise from assumptions made in the correction (Mroz et al., 2018; Marra et al., 2017; Le and Chandrasekar, 2021a).

3. Results

3.1. Characterization of hailstorms in the south of France coincident with DPR scans, 2014–2021

We examined eight hailstorms observed by DPR scans between 2014 and 2018, primarily the last three years. These occurred in the four study areas of France, predominantly in the Pyrenees. In these cases, there were between one and five impacted hailpads in the network, except for 20140628, on which there were nine such hailpads. Generally, the area of the storms was entirely observed by the Ku band and a significant portion of these areas by the Ka band. Only the storms of 20140628 and 20150418 were captured entirely by both frequency bands of the DPR, with their position coincident with the central scan footprints of the DPR swaths. There were two cases (20160607 and 20170807) in which the storms were in the outer part of the swath and therefore observed in their entirety only by the Ku band. This was because dual observation across the entire swath as not implemented until 2018.

Maximum values of the variables extracted from the DPR for each storm are shown in Table 3. The spatial distribution of these variables for each storm is depicted in Figs. 2–6. Table 3 shows that the maximum PRNS was mainly between 10 and 25 mm/h. Only three storms produced greater values: 20150418 (62 mm/h), 20160607 (106 mm/h), and 20170807 (88 mm/h). The pixels associated with the maximum PRNS values (Fig. 2) coincide with locations of the maximum zFFNS-Ku values (Fig. 3).

The zFFNS (Figs. 3 and 4) had larger values in the FSKu exploration than FSKa across all storms. The maximum zFFNS was between 45 and 55 dBZ in the Ku band and 37 and 45 dBZ in the Ka band, with a difference of 5–9 dBZ between the bands. However, on 20170807, zFFNS had a major difference between the two bands of the FS structure, which can be attributed to the storm's location outside the central footprints. In the events of 20140628, 20150418 and 20170807, FSKu values $\geq$ 50 dBZ (Table 3 and Figs. 3a, b, and e) were observed. Figs. 3 and 4 demonstrate how the Ku band detected storms with greater intensity and extent than the Ka band. On the other hand, zFF had values very similar to zFFNS in both bands (Table 3). In only two storms (20170807 and 20170823), the maximum values of zFF-Ku were greater than zFFNS-Ku. The maximum zFF-Ka value exceeded that of zFFNS-Ka in the 20140628 storm. Figs. 4 and 6 clearly indicate that the vertical structure of all convective storms was better captured using the Ku band.

Values of the variables calculated from DPR sensor data are shown in Table 4. The first column lists the HMR in both bands. According to the FS structure, values of this variable from Ku band generally extended below 1250 m, except in the two 2017 storms, for which it extended above 3500 m. In contrast, the Ka band produced maximum reflectivity values exclusively below 2500 m. On the other hand, the MHRRs of 40 and 45 dBZ were quite variable. The Ku band recorded a MHR40 between 6250 and 9375 m, except on 20160411, 20160607 and 20180430, whose values were below 3250 m, reflecting smaller vertical development (Figs. 5 and 6). The 45 dBZ MHRR was detected in a slightly lower maximum height range (5750–9125 m) than that of 40 dBZ with the Ku band, except on 20160607 and 20180404 when values were below 3875 m (Table 4, Fig. 5). The Ka band generated a greater number of cases in which these reference reflectivities were not detected, with only 40 dBZ reference values below 4375 m (Table 4, Fig. 6). The MHR50 was only detected in three Ku-band storms, in a range 3750–5125 m.

Distances between maximum heights of the three reference reflectivities (40, 45, and 50 dBZ) and heights of the 0° and –10 °C isotherms were also calculated (Table 4). The analysis was more thorough with the Ku band because the Ka band only reached 40 dBZ values, and these were only above those isotherms in the 20150418 case. With the Ku

Table 3
Maximum values of variables extracted from DPR for each storm.

Hailstorms	Spatial area analyzed (Km^2)	PRNS (mm/h)	zFFNS (dBZ)		zFF (dBZ)	
		FS	Ku	Ka	Ku	Ka
20140628	3600	25	50	42	50	43
20150418	3000	62	54	45	54	45
20160411	3750	14	45	40	45	40
20160607	12,500	106	46	39	46	39
20170807	7200	88	55	37	56	37
20170823	6175	18	48	39	52	39
20180404	2400	18	47	40	47	40
20180430	5775	10	45	37	45	37

Table 2
Description of selected hail detection algorithms (Mroz et al., 2017).

Algorithm formulae	Variables used	Threshold value
$Z_{Ku}^{mix} = 10\,log_{10}\left[\frac{\int_{-10°C}^{-10°C+4Km} Z(h)dh}{4Km}\right]$	-Z_{Ku}^{mix} :Mean Measured Reflectivity in mixed-phase layer (Ku band) (dBZ) -h: Height (m) -Z: Measured Reflectivity ($mm^6\,m^{-2}$)	$Z_{Ku}^{mix} > 40.42$
$Z_{KuKa}^{mix}\begin{cases} Z_{Ku}^{mix} > 0.632 Z_{Ka}^{mix} + 20.4 \\ Z_{Ku}^{mix} > 40.15 \end{cases}$	- Z_{Ka}^{mix} :Mean Measured Reflectivity in mixed-phase layer (Ka band) (dBZ) - Z_{KuKa}^{mix}: The two-variable algorithm, which includes the Mean Measured Reflectivity in mixed-phase layer (Ku and Ka band)	–
$Z_{Ku}^{int} = 10\,log_{10}\int_{FLH}^{CTH} Z(h)dh$	-Z_{Ku}^{int} :The column-integrated Measured Reflectivity (Ku band) (dBZ) -CTH: Cloud-Top Height (m) -FLH: Freezing Level Height (m). -h: Height (m) -Z: Measured Reflectivity ($mm^6\,m^{-2}$)	$Z_{Ku}^{int} > 79.32$
–	-$H40_{Ku}^{AFL}$:The 40-dBZ Measured Reflectivity-level height above the 0 °C isotherm (Ku band) (km) -AFL: Above Freezing Level	$H40_{Ku}^{AFL} > 3.26$
–	-$H30_{Ka}^{AFL}$:The 30-dBZ Measured Reflectivity-level height above the 0 °C isotherm (Ka band) (km) -AFL: Above Freezing Level	$H30_{Ka}^{AFL} > 5.23$

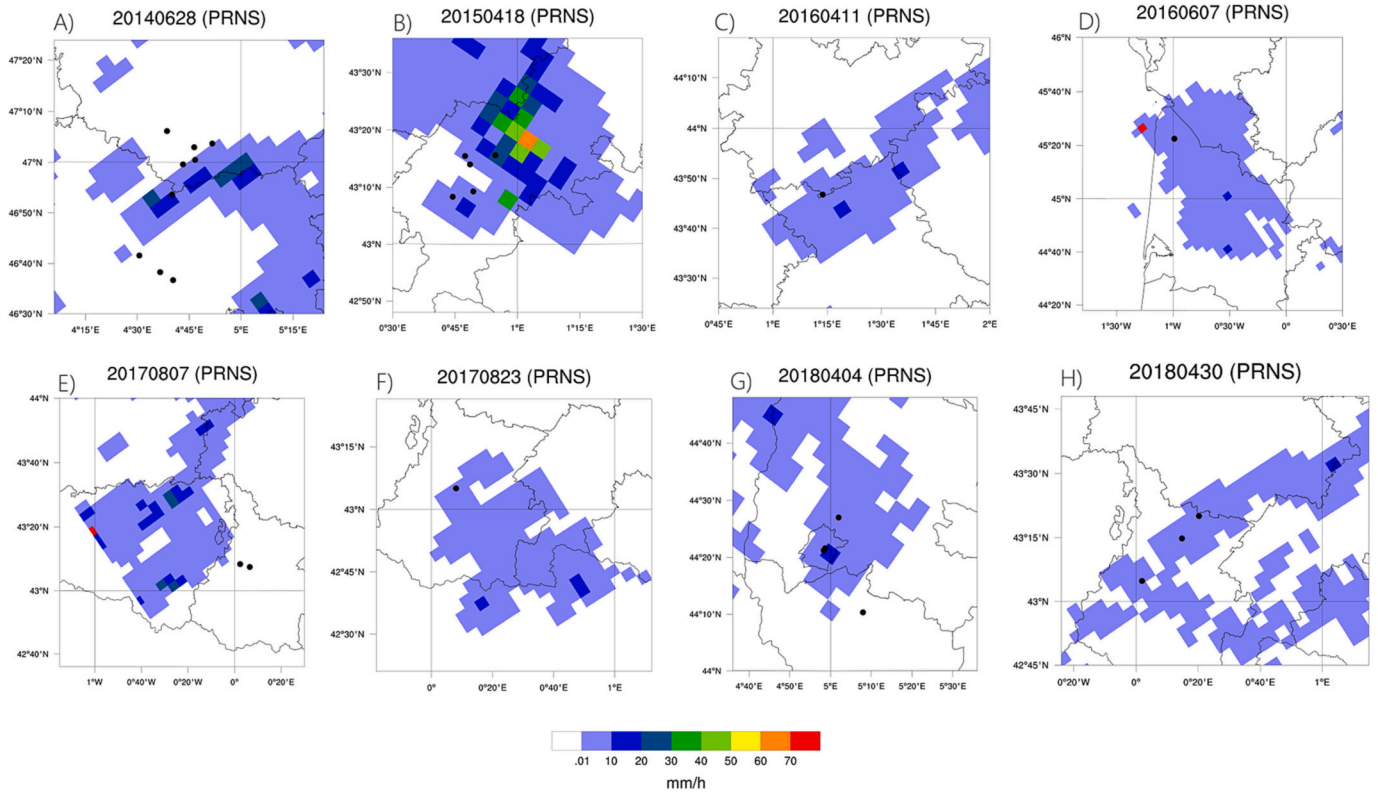

Fig. 2. Precipitation Rate Near Surface (PRNS) extracted from FS structure-DPR. Black dots represent hailpads impacted and coincident with the DPR scan for each storm.

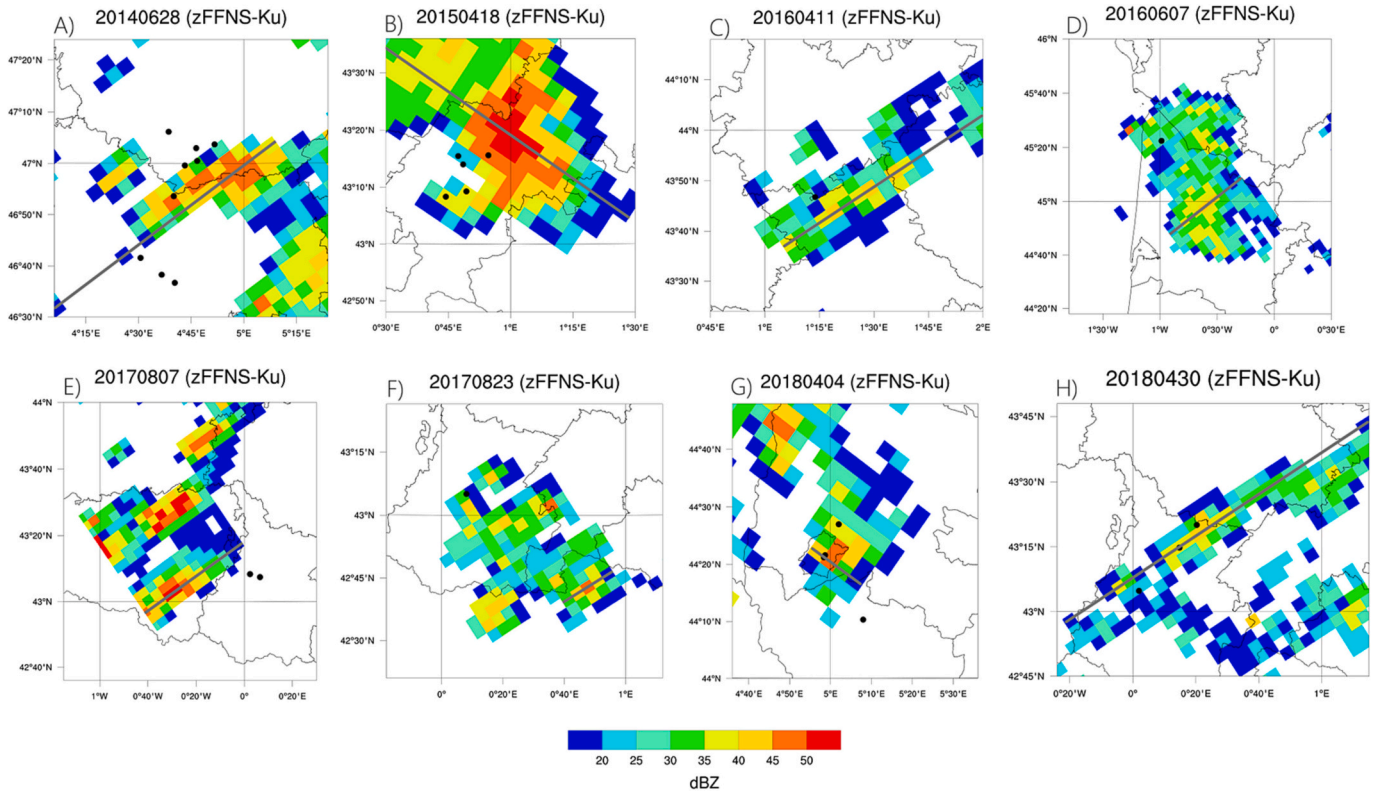

Fig. 3. Corrected Reflectivity Factor Near Surface (zFFNS-Ku) extracted from FS structure-DPR. Black dots represent hailpads impacted and coincident with the DPR scan for each storm. The gray line shows the location of the vertical cross-sections displayed in Fig. 5.

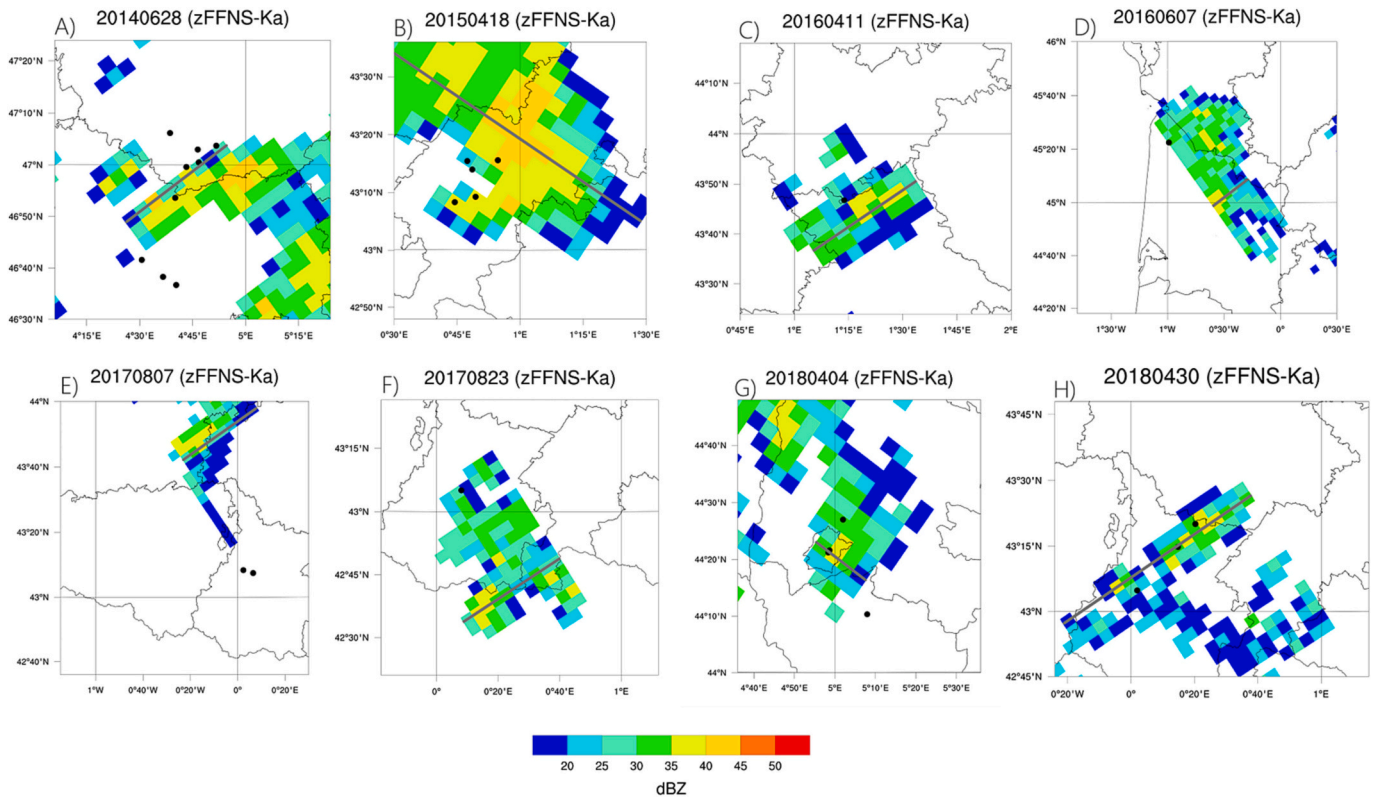

Fig. 4. Corrected Reflectivity Factor Near Surface (zFFNS-Ka) extracted from FS structure-DPR. Black dots represent hailpads impacted and coincident with the DPR scan for each storm. The gray line shows the location of the vertical cross-sections displayed Fig. 6.

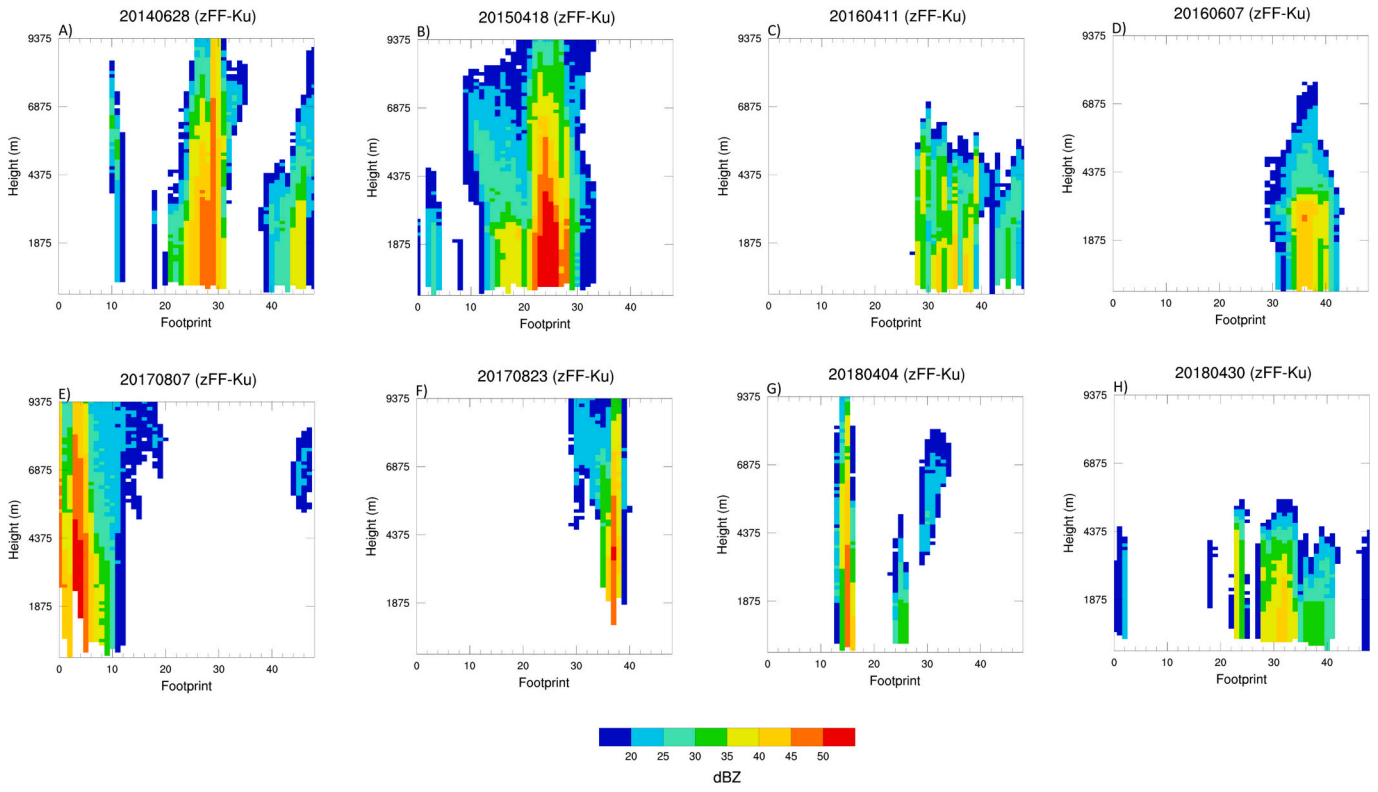

Fig. 5. Vertical cross-section of Corrected Reflectivity Factor (zFF-Ku) extracted from FS structure-DPR.

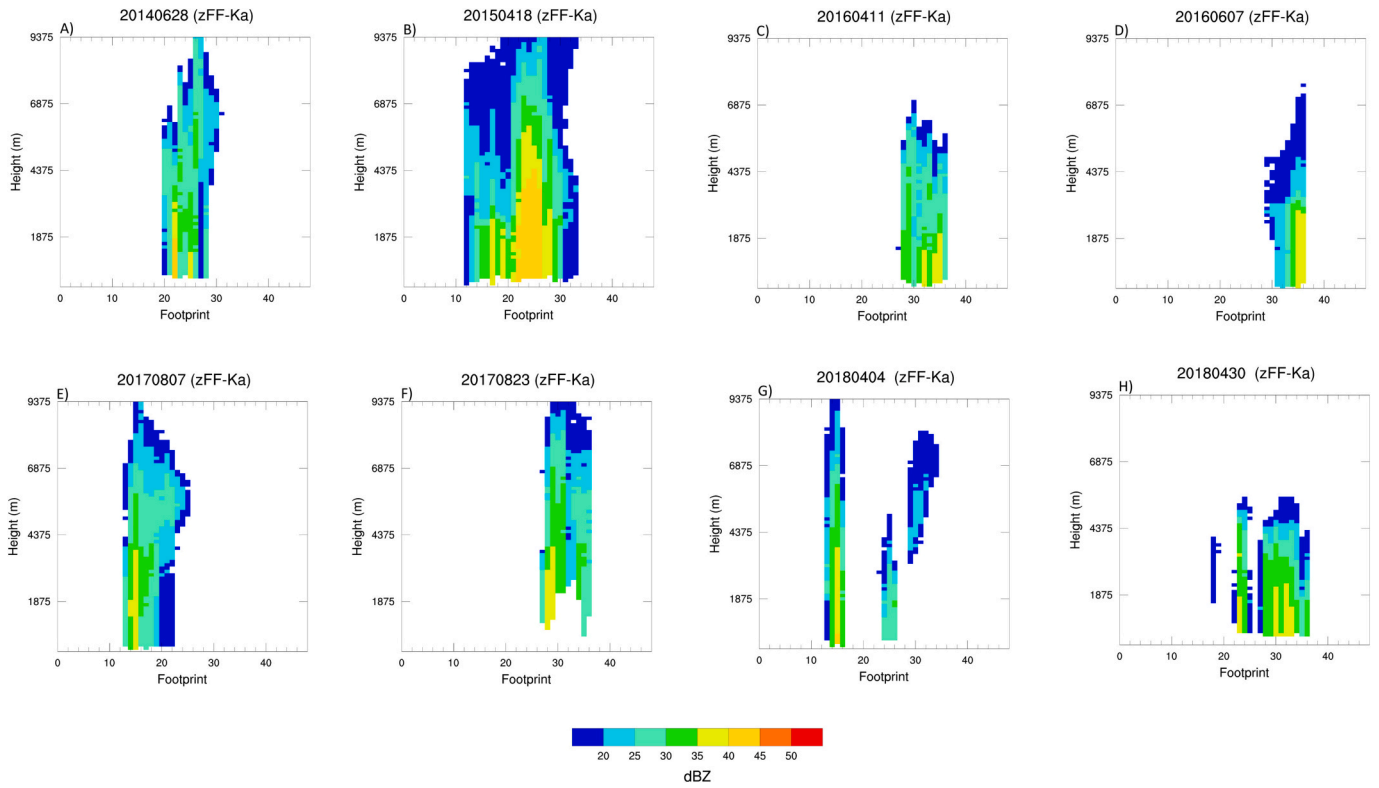

Fig. 6. Vertical cross-section of Corrected Reflectivity Factor (zFF-Ka) extracted from FS structure-DPR.

Table 4
Variables retrieved from DPR sensor for each storm. Red values represent instances when reference reflectivity values are attained below the isotherms.

Hailstorms	*HMR (m)*		*MHR40 (m)*		*MHR45 (m)*		*MHR50 (m)*		*DMH40Ku (m)*		*DMH45Ku (m)*		*DMH50Ku (m)*		*DMH40Ka (m)*	
	Ku	***Ka***	***Ku***	***Ka***	***Ku***	***Ka***	***Ku***	***Ka***	***0º***	***−10º***	***0º***	***−10º***	***0º***	***−10º***	***0º***	***−10º***
20140628	375/500	1250	9250	3375	7125	-	-	-	5766	4012	3641	1887	-	-	109	1863
20150418	375/1125	375	6500	4375	5750	-	3750	-	3900	2377	3150	1627	1150	373	1775	252
20160411	125/1000	125-250	2125	-	-	-	-	-	125	1534	-	-	-	-	-	-
20160607	625	2500	3250	-	2750	-	-	-	565	2113	1065	2613	-	-	-	-
20170807	4250	125	9375	-	9125	-	5125	-	4914	3752	4664	3502	664	498	-	-
20170823	3500	1250	8375	-	5750	-	3875	-	3909	2773	1284	148	591	1727	-	-
20180404	500/1250	250	6250	500	3875	-	-	-	4000	2465	1625	90	-	-	1750	3285
20180430	625/1000	1375	2875	-	-	-	-	-	1328	177	-	-	-	-	-	-

band, the reference values (40 and 45 dBZ) were detected below both isotherms in a single case (20160607). In the remaining cases, the reference reflectivities were recorded above the freezing level, except for the 50 dBZ value in the 20170823 storm, which was around 600 m below that level. For the −10 °C isotherm, the 40 dBZ value was observed below that level in two additional cases, and in no case was 50 dBZ detected above that level.

Table 5 show the maximum values of ANELFA surface variables as determined in the eight hailstorms. Because of their severity and damage caused in the study area, days 20140628, 20150418 and 20170807 were classified by ANELFA as major hail events in the corresponding campaigns. On 20140628, 28-mm diameter hailstones reached the surface with a kinetic energy of fall at 346.7 J/m^2. On 20150418, there were considerable values of the four parameters analyzed. A hail number of 18,556 m^{-2} was detected by one of the sensors, with a mass of 3461 g and kinetic energy of 266.9 J m^{-2}. On another hailpad there were

Table 5
Maximum values of surface hail (ANELFA).

Hailstorms detected by DPR	*Maximum diameter (mm)*	*Maximum total number (/m^2)*	*Maximum mass (g/m^2)*	*Maximum kinetic energy of fall (J/m^2)*
20140628	28	2251	1828	346.7
20150418	19	18,556	3461	266.9
20160411	11	684	126	9.6
20160607	5	20	2	0.1
20170807	18	10,602	2404	222.7
20170823	11	451	86	6.5
20180404	18	5348	1688	167.2
20180430	8	18,807	1705	94.6

impacts of hailstones up to 19 mm in diameter. Finally, on day 20170807 the maximum values were smaller than in the previous case. Furthermore, data obtained from the DPR confirmed that these three storms had greater vertical development, with greater reflectivities than in the other storms.

3.2. Hail detection using DPR data

Five hail prediction algorithms (Table 2, Mroz et al., 2017) were evaluated for the main convective cells of the eight storms. The spatial results of the algorithms for each case study are depicted in Fig. 7, except 20160411 and 20160607 cases, where no algorithm sensed hail. These algorithms were $Z_{\mathrm{Ku}}^{\mathrm{mix}}$:Mean Measured Reflectivity in mixed-phase layer (Ku band); Z_{KuKa}^{mix} :the two-variable algorithm which includes the Mean Measured Reflectivity in mixed-phase layer (Ku and Ka band); Z_{Ku}^{int} :Column-integrated Measured Reflectivity (Ku band); $H40_{Ku}^{AFL}$:The 40-dBZ Measured Reflectivity-level height above the 0 °C isotherm (Ku band) and $H30_{Ka}^{AFL}$:The 30-dBZ Measured Reflectivity-level height above the 0 °C isotherm (Ka band).

For the 20140628 storm, all algorithms detected hail, though with significant spatial differences. The $H40_{Ku}^{AFL}$ algorithm indicated hail over the largest area (six pixels), while the $H30_{Ka}^{AFL}$ algorithm detected hail in just two pixels. The Z_{Ku}^{mix} and Z_{Ku}^{int} algorithms showed hail in 5 pixels, and Z_{KuKa}^{mix}in four. In the 20150418 storm, all algorithms detected hail except for $H30_{Ka}^{AFL}$. The location and extent of hail-detection areas were similar among the algorithms.

For the 20170807 storm, there was great variability in hail detection by the algorithms. Algorithms based on Ku band data indicated the largest hail area of all cases (7–12 pixels), while the two algorithms involving Ka band variables did not detect this hydrometeor. It was similar for the 20170823 case, with one spatially coincident pixel in the three algorithms based on Ku-band data and no detection by the Ka-band algorithms.

In the 20180404 storm, all algorithms showed hail with similar spatial areas (2–3 pixels) and locations, except for the $H30_{Ka}^{AFL}$ algorithm, which did not detect hail. In the last storm of 20180430, the only algorithm that detected hail was Z_{Ku}^{int} (six pixels). Finally, in the 20160411 and 20160607 cases, no algorithm sensed hail in the analyzed convective cells.

In summary, algorithms based on the Ka band produced smaller hail detection areas than those based on Ku band, although the Ka band only captured the entirety of convective cells in the 20140628 and 20150418 cases. Thus, the algorithms that showed a larger hail extent were $Z_{Ku}^{int}$and $H40_{Ku}^{AFL}$ (average 2.9 pixels), closely followed by Z_{Ku}^{mix} (average 2.6 pixels). In 6 of the 8 cases, the Ku band-based algorithms detected hail, with the storm's smaller vertical development the main limiting factor for non-detection in the remaining two cases.

4. Discussion

Characterization of the eight hailstorms in France by the DPR during 2014–2021 shows the utility of the GPM observations for hailstorm detection. Hailfalls at the surface were verified using the ANELFA hailpad network, highlighting the advantages of these direct surface observations in severe weather monitoring (Melcón et al., 2017; Sánchez et al., 2017). Use of these data as ground truth differs from the most recent research based on NASA's terrestrial validation program, which includes of a network of S-band Doppler radars (Next-Generation Radar) in the United States (Mroz et al., 2017 and 2018; Seiki, 2021, and Le & Chandrasekar, 2021a and 2021b). Although direct observation networks do not provide spatially continuous data on hail because of the short duration and isolated nature of these measurements, they do permit the acquisition of objective and unbiased information about hail at the surface and its characteristics. Our research in an area of Europe where hail behavior is different mainly because of the orography and circulation patterns (Punge and Kunz, 2016) can contribute to the global analysis of hailstorms using GPM data.

Data from both radar frequencies (Ku and Ka) were used in the hailstorm analysis. To improve DPR detection capabilities, Mroz et al. (2017, 2018) stated that Ku band measurements should be used and, in parallel, complementary observations of the Ka band. It should be noted that the DPR data for characterizing hail events were acquired from previous studies, demonstrating the ability of these radar parameters to detect hydrometeors. Among those, Donaldson Jr. (1959) should be mentioned. He showed that hail occurrence was strongly related to the maximum reflectivity, using 50 dBZ as a reference. Additionally, Waldvogel et al. (1979) used a maximum echo height of 45 dBZ from X band as a measure of updraft velocity in convective thunderstorms. Depue et al. (2007) proposed an algorithm using S-band polarimetric radar reflectivity and differential reflectivity values, which had a critical success rate of 77%. Likewise, López and Sánchez (2009) used C-band radar data showing that the maximum reflectivity factor and height of maximum reflectivity contributed positively in two statistical models of hail detection. Recently, Le and Chandrasekar (2021b) developed a hail identification algorithm with data such as maximum reflectivity from Ku.

Analysis of the near-surface precipitation rate using the dual-frequency pattern revealed that three of the identified storms exceeded 50 mm/h, with one surpassing 100 mm/h. The remaining storms showed very small maxima (< 25 mm/h). However, according to Kubota et al. (2014) and Toyoshima et al. (2015), there is underestimation of precipitation when observed using the Ka band. Furthermore, Mroz et al. (2018) suggested that hail can affect the accuracy of DPR rain rate estimates because it amplifies multiple scattering in the Ka band.

According to Biswas and Chandrasekar (2018) and Michaelides (2019), the DPR reflectivity factor is the most important parameter obtained from the observations. Therefore, in our investigation, attenuation-corrected reflectivities of the final processing module were used to characterize the eight storms. This was despite substantial uncertainty and ambiguities surrounding the attenuation correction in the Ku and Ka bands (Mroz et al., 2018), mainly in intense storms. There are other criteria such as those of Seiki (2021), who asserted that the use of attenuation-corrected reflectivity mitigates the effect of dispersion and is more effective in classifying hydrometeors.

The reflectivity factor obtained with the Ku band more clearly characterizes the vertical structure and intensity of storms. However, maximum reflectivity in all cases from the Ka band was weaker than that from Ku band. This is also reflected by Mroz et al. (2017), in which they suggested that large hailstones scatter the Ka band signal (Mie scattering), thus hindering detection of that hydrometeor. Additionally, even when using corrected reflectivity, the Ka- band profile can still be affected.

Maximum reflectivities registered with the Ku band near the surface and/or in the vertical column were ≥ 50 dBZ in four of the storms, i.e., 20140628, 20150418, 20170807, and 20170823. On the other hand, with the Ka band, these same storms had values 37–45 dBZ, depending on the storm area observed at this frequency. According to Waldvogel et al. (1979), extreme values of reflectivity are considered a satisfactory criterion for the detection of hail. In general, the maximum reflectivity observed in the Ku band exceeded 43 dBZ. Given this, Cecil (2009) used radar measurements from the TRMM satellite (Ku band) to conclude that 74% of storms with an echo of 49.1 dBZ and 43% with 43.1 dBZ at an altitude of 9 km were associated with surface hail records.

In the storms analyzed, the height of maximum reflectivity showed strong variability among cases, preventing the establishment of specific thresholds. The maximum heights for reference reflectivities (40, 45, and 50 dBZ) could only be determined using the Ku band, because values were smaller in most cases with the Ka band. Thus, a maximum height between 5700 and 9300 m for reflectivities of 40 and 45 dBZ and 3700–5200 m for 50 dBZ was observed. Moreover, reflectivities of 40,

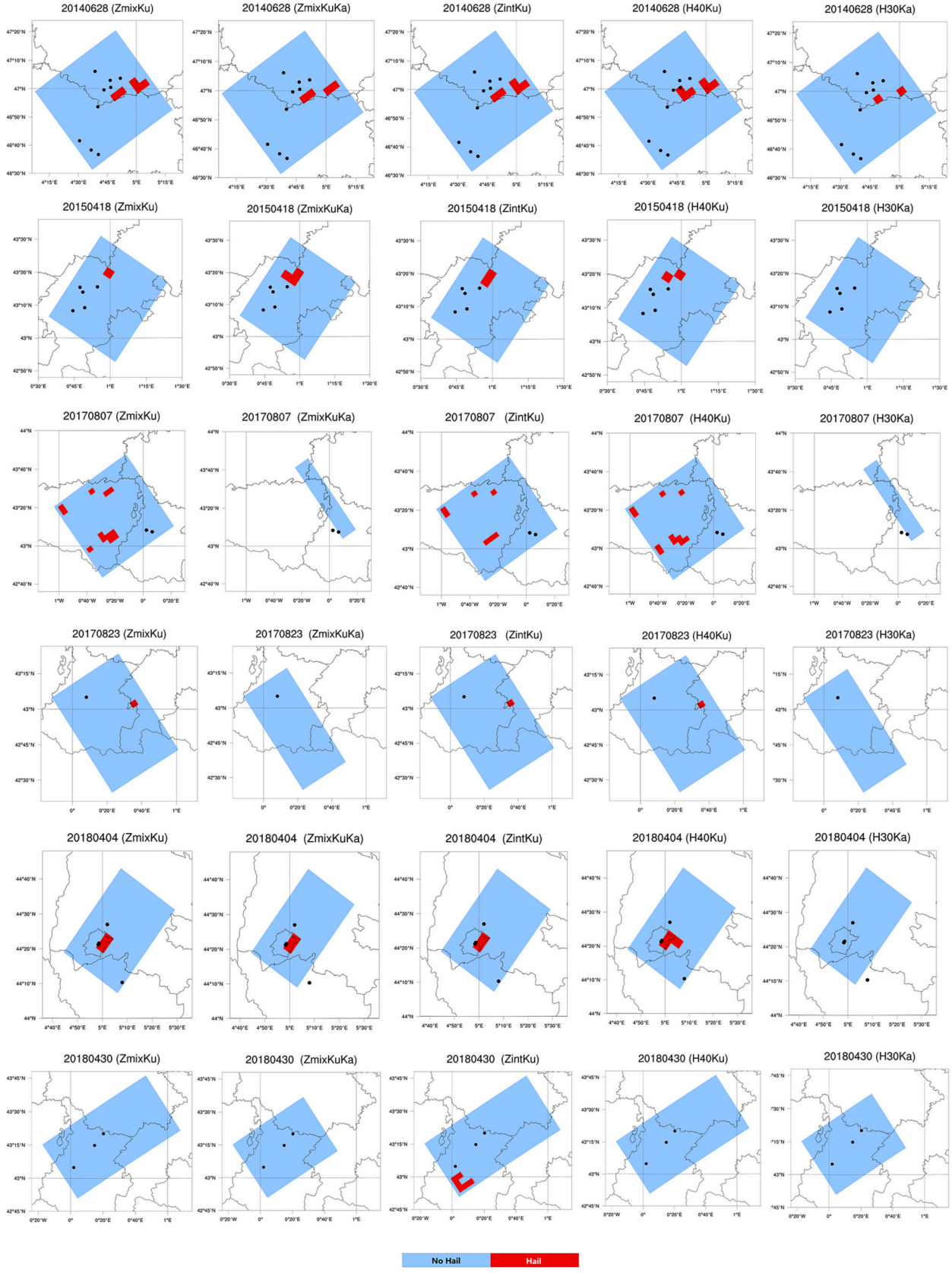

Fig. 7. Evaluation of five hail detection algorithms using DPR variables, adapted from Mroz et al. (2017). Black dots represent hailpads impacted and coincident with the DPR scan for each storm. Red pixels indicate hail detection and blue pixels an absence of these hydrometeors. (For interpretation of the references to colour in this figure legend, the reader is referred to the web version of this article.)

45, and 50 dBZ in the Ku band were obtained in most cases above the freezing level. Similarly, this was observed with respect to the −10 °C isotherm, albeit in fewer storms and with the exception that 50 dBZ was below this isotherm in all cases. In contrast, in the Ka band, only 40 dBZ was reached in some storms and at lower levels. According to Mroz et al. (2017, 2018), the maximum height of measured reflectivity 40 dBZ above the 0 °C isotherm is a strong indicator of hail in the Ku band and has a significant correlation with the tropopause height. This is unlike the Ka band, for which dispersion processes make it difficult to detect hail. Moreover, a study using TRMM data (Ku band) verified that 40-dBZ echo at high altitudes indicated an intense storm with strong updrafts (Zipser et al., 2006).

Finally, evaluation of the five hail detection algorithms developed by Mroz et al. (2017) yielded general results indicating that in two of the eight storms (20160411 and 20160607), no hail was detected by any algorithm, and only in 20140628 did all algorithms detect hail. It should be noted that part of the storm area was not observed by the Ka band, which could have influenced results of the algorithms that include variables of this frequency. Thus, the algorithms including variables from the Ku band detected a greater number of pixels with hail. Mroz et al. (2017) asserted that parameters related to the reflectivity factor of Ku band are the most effective hail indicators, with high critical success rates. However, the two-variable algorithm is the most effective, despite the disadvantage of being evaluated over a smaller area in six of the eight identified storms. This was because the Ka band only completely observed the 20140628 and 20150418 storms.

We concur with Marra et al. (2017) that the use of GPM data should increasingly be oriented toward investigating the dynamics of extreme events in various regions of the planet. Therefore, the characterization of the French hailstorms during 2014–2021 based on DPR observation can contribute to future work. Furthermore, according to Punge and Kunz (2016), they can improve the monitoring and prediction of hailstorms in Europe.

5. Conclusions

Eight hailstorm events over France from 2014 to 2021 were analyzed using observations from the DPR-GPM and ground-based observations from ANELFA. The research reaffirmed the utility of hailpad networks for pinpoint verification of hailfall on the ground.

The Ku band demonstrated greater capacity in identifying hailstorms. Storms with larger reflectivity values ($\geq$ 50 dBZ, Ku band), both near the surface and throughout the vertical column, were those with a more clearly defined vertical structure and thus more powerful convective development. The intensity of these hailstorms was confirmed with ground-based data from ANELFA.

The height of maximum reflectivity was not a particularly useful variable for establishing thresholds or behavioral patterns of hailstorms because of highly variable results. Maximum heights for the reference reflectivities of 40 and 45 dBZ found via Ku band were 5700–9300 m and 3700–5200 m for 50 dBZ. With the Ka band, it was impossible to establish altitude ranges for the three reflectivities, because 40 dBZ was attained only in a few storms. Additionally, those reflectivities in the Ku band were observed in most cases above the freezing level. This was also seen for the −10 °C isotherm, except for 50-dBZ values found below this isotherm in all cases. In contrast, the Ka band only reached 40 dBZ in some storms at lower levels.

The assessment of the five hail detection algorithms of Mroz et al. (2017) confirms that algorithms incorporating variables from Ku band detect a greater number of hail-containing pixels, primarily for storms that were intense according to substantial values of both satellite and ground-based observations. The two-variable algorithm deemed most effective by Mroz et al. (2017) could not be adequately evaluated in our study because the Ka band only fully observed the area of the main convective cell in two storms. Further case studies from 2018 onwards, following a change in the DPR sensor scan pattern that allowed dual-frequency observation of the same spatial region, will enable more comprehensive evaluations of the algorithms in future.

CRediT authorship contribution statement

Laura Rivero-Ordaz: Writing – original draft, Validation, Software, Methodology, Investigation, Formal analysis, Data curation, Conceptualization. **Andrés Navarro:** Resources, Methodology, Investigation. **Francisco J. Tapiador:** Project administration, Investigation, Funding acquisition. **José L. Sánchez:** Resources, Investigation. **Eduardo García-Ortega:** Writing – review & editing, Visualization, Supervision, Project administration, Methodology, Investigation, Funding acquisition, Formal analysis, Conceptualization.

Declaration of competing interest

The authors declare that they have no known competing financial interests or personal relationships that could have appeared to influence the work reported in this paper.

Data availability

Data will be made available on request.

Acknowledgements

Funding came from projects PID2019-108470RB-C22, PID2019-108470RB-C21 and PID2022-1382980B-C21, funded by MCIN/AEI/10.13039/501100011033. The authors acknowledge the association ANELFA, in particular Jean Dessens and Claude Berthet.

Appendix A. Supplementary data

Supplementary data to this article can be found online at https://doi.org/10.1016/j.atmosres.2024.107308.

References

Auer Jr., A.H., 1994. Hail recognition through the combined use of radar reflectivity and cloud-top temperatures. Mon. Weather Rev. 122 (9), 2218–2221. https://doi.org/10.1175/1520-0493(1994)122<2218:HRTTCU>2.0.CO;2.

Bang, S.D., Cecil, D.J., 2019. Constructing a multifrequency passive microwave hail retrieval and climatology in the GPM domain. J. Appl. Meteorol. Climatol. 58 (9), 1889–1904. https://doi.org/10.1175/JAMC-D-19-0042.1.

Bang, S.D., Cecil, D.J., 2021. Testing passive microwave-based hail retrievals using GPM DPR Ku-band radar. J. Appl. Meteorol. Climatol. 60 (3), 255–271. https://doi.org/10.1175/JAMC-D-20-0129.1.

Berthet, C., Wesolek, E., Dessens, J., Sanchez, J.L., 2013. Extreme hail day climatology in Southwestern France. Atmos. Res. 123, 139–150. https://doi.org/10.1016/j.atmosres.2012.10.007.

Biswas, S.K., Chandrasekar, V., 2018. Cross-validation of observations between the GPM dual-frequency precipitation radar and ground based dual-polarization radars. Remote Sens. 10 (11), 1773. https://doi.org/10.3390/rs10111773.

Cecil, D.J., 2009. Passive microwave brightness temperatures as proxies for hailstorms. J. Appl. Meteorol. Climatol. 48 (6), 1281–1286. https://doi.org/10.1175/2009JAMC2125.1.

Depue, T.K., Kennedy, P.C., Rutledge, S.A., 2007. Performance of the hail differential reflectivity (HDR) polarimetric radar hail indicator. J. Appl. Meteorol. Climatol. 46 (8), 1290–1301. https://doi.org/10.1175/JAM2529.1.

Donaldson Jr., R.J., 1959. Analysis of severe convective storms observed by radar-II. J. Atmos. Sci. 16 (3), 281–287. https://doi.org/10.1175/1520-0469(1959)016<0281:AOSCSO>2.0.CO;2.

Doswell III, C.A., 1987. The distinction between large-scale and mesoscale contribution to severe convection: a case study example. Weather Forecast. 2 (1), 3–16. https://doi.org/10.1175/1520-0434(1987)002<0003:TDBLSA>2.0.CO;2.

Heinselman, P.L., Ryzhkov, A.V., 2006. Validation of polarimetric hail detection. Weather Forecast. 21 (5), 839–850. https://doi.org/10.1175/WAF956.1.

Hermida, L., Sánchez, J.L., López, L., Berthet, C., Dessens, J., García-Ortega, E., Merino, A., 2013. Climatic trends in hail precipitation in France: spatial, altitudinal, and temporal variability. Sci. World J. https://doi.org/10.1155/2013/494971.

Hou, A.Y., Kakar, R.K., Neeck, S., Azarbarzin, A.A., Kummerow, C.D., Kojima, M., Oki, R., Nakamura, K., Iguchi, T., 2014. The global precipitation measurement mission. Bull. Am. Meteorol. Soc. 95 (5), 701–722. https://doi.org/10.1175/BAMS-D-13-00164.1.

Iguchi, T., Meneghini, R., 2021. GPM DPR Precipitation Profile L2A 1.5 hours 5 km V07. Earth Sciences Data and Information Services Center (GES DISC), Greenbelt, MD, Goddard. https://doi.org/10.5067/GPM/DPR/GPM/2A/07. Acceso: [24/05–30/08/2022].

Johns, R.H., Doswell III, C.A., 1992. Severe local storms forecasting. Weather Forecast. 7 (4), 588–612. https://www.researchgate.net/profile/Charles-Doswell-Iii/publication/260894939_Severe_Local_Storms_Forecasting/links/55c12e8808aed621de1541cd/Severe-Local-Storms-Forecasting.pdf.

Kidd, C., Levizzani, V., 2011. Status of satellite precipitation retrievals. Hydrol. Earth Syst. Sci. 15 (4), 1109–1116. https://doi.org/10.5194/hess-15-1109-2011.

Kidd, C., Becker, A., Huffman, G.J., Muller, C.L., Joe, P., Skofronick-Jackson, G., Kirschbaum, D.B., 2017. So, how much of the Earth's surface is covered by rain gauges? Bull. Am. Meteorol. Soc. 98 (1), 69–78. https://doi.org/10.1175/BAMS-D-14-00283.1.

Kitzmiller, D.H., McGovern, W.E., Saffle, R.F., 1995. The WSR-88D severe weather potential algorithm. Weather Forecast. 10 (1), 141–159. https://doi.org/10.1175/1520-0434(1995)010<0141:TWSWPA>2.0.CO;2.

Kubota, T., Yoshida, N., Urita, S., Iguchi, T., Seto, S., Meneghini, R., Awaka, J., Hanado, H., Kida, S., Oki, R., 2014. Evaluation of precipitation estimates by at-launch codes of GPM/DPR algorithms using synthetic data from TRMM/PR observations. IEEE J. Sel. Top. Appl. Earth Obs. Remote Sens. 7 (9), 3931–3944. https://doi.org/10.1109/JSTARS.2014.2320960.

Kunz, M., 2007. The skill of convective parameters and indices to predict isolated and severe thunderstorms. Nat. Hazards Earth Syst. Sci. 7 (2), 327–342. https://doi.org/10.5194/nhess-7-327-2007.

Laviola, S., Monte, G., Levizzani, V., Ferraro, R.R., Beauchamp, J., 2020. A new method for hail detection from the GPM constellation: a prospect for a global hailstorm climatology. Remote Sens. 12 (21), 3553. https://doi.org/10.3390/rs12213553.

Le, M., Chandrasekar, V., 2021a. Graupel and hail identification algorithm for the dual-frequency precipitation radar (DPR) on the GPM core satellite. J. Meteorol. Soc. Jpn. Ser. II https://doi.org/10.2151/jmsj.2021-003.

Le, M., Chandrasekar, V., 2021b. A new hail product for GPM DPR. In: 2021 IEEE International Geoscience and Remote Sensing Symposium IGARSS. IEEE, pp. 828–831.

López, L., Sánchez, J.L., 2009. Discriminant methods for radar detection of hail. Atmos. Res. 93 (1–3), 358–368. https://doi.org/10.1016/j.atmosres.2008.09.028.

López, L., García-Ortega, E., Sánchez, J.L., 2007. A short-term forecast model for hail. Atmos. Res. 83 (2–4), 176–184. https://doi.org/10.1016/j.atmosres.2005.10.014.

Marra, A.C., Porcù, F., Baldini, L., Petracca, M., Casella, D., Dietrich, S., Mugnai, A., Sanò, P., Vulpiani, G., Panegrossi, G., 2017. Observational analysis of an exceptionally intense hailstorm over the Mediterranean area: role of the GPM Core Observatory. Atmos. Res. 192, 72–90. https://doi.org/10.1016/j.atmosres.2017.03.019.

Melcón, P., Merino, A., Sánchez, J.L., López, L., García-Ortega, E., 2017. Spatial patterns of thermodynamic conditions of hailstorms in southwestern France. Atmos. Res. 189, 111–126. https://doi.org/10.1016/j.atmosres.2017.01.011.

Michaelides, S., 2019. Editorial for special issue "remote sensing of precipitation". Remote Sens. 11 (4), 389. https://doi.org/10.3390/rs11040389.

Mroz, K., Battaglia, A., Lang, T.J., Cecil, D.J., Tanelli, S., Tridon, F., 2017. Hail-detection algorithm for the GPM Core Observatory satellite sensors. J. Appl. Meteorol. Climatol. 56 (7), 1939–1957. https://doi.org/10.1175/JAMC-D-16-0368.1.

Mroz, K., Battaglia, A., Lang, T.J., Tanelli, S., Sacco, G.F., 2018. Global precipitation measuring dual-frequency precipitation radar observations of hailstorm vertical structure: current capabilities and drawbacks. J. Appl. Meteorol. Climatol. 57 (9), 2161–2178. https://doi.org/10.1175/JAMC-D-18-0020.1.

Ni, X., Liu, C., Cecil, D.J., Zhang, Q., 2017. On the detection of hail using satellite passive microwave radiometers and precipitation radar. J. Appl. Meteorol. Climatol. 56 (10), 2693–2709. https://doi.org/10.1175/JAMC-D-17-0065.1.

Ortega, K.L., Krause, J.M., Ryzhkov, A.V., 2016. Polarimetric radar characteristics of melting hail. Part III: validation of the algorithm for hail size discrimination. J. Appl. Meteorol. Climatol. 55 (4), 829–848. https://doi.org/10.1175/JAMC-D-15-0203.1.

Panegrossi, G., Casella, D., Dietrich, S., Marra, A.C., Sanò, P., Mugnai, A., Baldini, L., Roberto, N., Adirosi, E., Cremonini, R., Bechini, R., Vulpiani, G., Petracca, M., Porcù, F., 2016. Use of the GPM constellation for monitoring heavy precipitation events over the Mediterranean region. IEEE J. Sel. Top. Appl. Earth Obs. Remote Sens. 9 (6) https://doi.org/10.1109/JSTARS.2016.2520660, 2733–27.

Punge, H.J., Kunz, M., 2016. Hail observations and hailstorm characteristics in Europe: a review. Atmos. Res. 176, 159–184. https://doi.org/10.1016/j.atmosres.2016.02.012.

Sánchez, J.L., Marcos, J.L., Dessens, J., López, L., Bustos, C., García-Ortega, E., 2009. Assessing sounding-derived parameters as storm predictors in different latitudes. Atmos. Res. 93 (1–3), 446–456. https://doi.org/10.1016/j.atmosres.2008.11.006.

Sánchez, J.L., Merino, A., Melcón, P., García-Ortega, E., Fernández-González, S., Berthet, C., Dessens, J., 2017. Are meteorological conditions favoring hail precipitation change in Southern Europe? Analysis of the period 1948–2015. Atmos. Res. 198, 1–10. https://doi.org/10.1016/j.atmosres.2017.08.003.

Seiki, T., 2021. Near-global three-dimensional hail signals detected by using GPM-DPR observations. J. Meteorol. Soc. Jpn. Ser. II. https://doi.org/10.2151/jmsj.2021-018.

Smith, P.L., Waldvogel, A., 1989. On determinations of maximum hailstone sizes from hailpad observations. J. Appl. Meteorol. (1988–2005) 28 (1), 71–76. http://www.jstor.org/stable/26183711.

Toker, E., Ezber, Y., Sen, O.L., 2021. Numerical simulation and sensitivity study of a severe hailstorm over Istanbul. Atmos. Res. 250, 105373 https://doi.org/10.1016/j.atmosres.2020.105373.

Toyoshima, K., Masunaga, H., Furuzawa, F.A., 2015. Early evaluation of Ku-and Ka-band sensitivities for the global precipitation measurement (GPM) dual-frequency precipitation radar (DPR). Sola 11, 14–17. https://doi.org/10.2151/sola.2015-004.

Waldvogel, A., Schmid, W., Federer, B., 1978. The kinetic energy of hailfalls. Part I: hailstone spectra. J. Appl. Meteorol. (1962–1982) 17 (4), 515–520. http://www.jstor.org/stable/26178483.

Waldvogel, A., Federer, B., Grimm, P., 1979. Criteria for the detection of hail cells. J. Appl. Meteorol. Climatol. 18 (12), 1521–1525. https://doi.org/10.1175/1520-0450(1979)018<1521:CFTDOH>2.0.CO;2.

Witt, A., Eilts, M.D., Stumpf, G.J., Johnson, J.T., Mitchell, E.D.W., Thomas, K.W., 1998. An enhanced hail detection algorithm for the WSR-88D. Weather Forecast. 13 (2), 286–303. https://doi.org/10.1175/1520-0434(1998)013<0286:AEHDAF>2.0.CO;2.

Zipser, E.J., Cecil, D.J., Liu, C., Nesbitt, S.W., Yorty, D.P., 2006. Where are the most intense thunderstorms on earth? Bull. Am. Meteorol. Soc. 87 (8), 1057–1072. https://doi.org/10.1175/BAMS-87-8-1057.